Observation of Polarization Vortices in Momentum Space

Yiwen Zhang,[1,4] Ang Chen,[1,4] Wenzhe Liu,[1,4] Chia Wei Hsu,[3] Bo Wang,[1,4] Fang Guan,[1,4] Xiaohan Liu,[1,4] Lei Shi,[1,4,*] Ling Lu,[2,†] and Jian Zi[1,4,‡]

[1]*Department of Physics, Key Laboratory of Micro- and Nano-Photonic Structures (Ministry of Education), and State Key Laboratory of Surface Physics, Fudan University, Shanghai 200433, China*

[2]*Institute of Physics, Chinese Academy of Sciences/Beijing National Laboratory for Condensed Matter Physics, Beijing 100190, China*

[3]*Department of Applied Physics, Yale University, New Haven, Connecticut 06520, USA*

[4]*Collaborative Innovation Center of Advanced Microstructures, Fudan University, Shanghai 200433, China*

(Received 2 November 2017; published 4 May 2018)

The vortex, a fundamental topological excitation featuring the in-plane winding of a vector field, is important in various areas such as fluid dynamics, liquid crystals, and superconductors. Although commonly existing in nature, vortices were observed exclusively in real space. Here, we experimentally observed momentum-space vortices as the winding of far-field polarization vectors in the first Brillouin zone of periodic plasmonic structures. Using homemade polarization-resolved momentum-space imaging spectroscopy, we mapped out the dispersion, lifetime, and polarization of all radiative states at the visible wavelengths. The momentum-space vortices were experimentally identified by their winding patterns in the polarization-resolved isofrequency contours and their diverging radiative quality factors. Such polarization vortices can exist robustly on any periodic systems of vectorial fields, while they are not captured by the existing topological band theory developed for scalar fields. Our work provides a new way for designing high-Q plasmonic resonances, generating vector beams, and studying topological photonics in the momentum space.

DOI: 10.1103/PhysRevLett.120.186103

The winding of a vector field in two dimensions forms a vortex whose core is located at the field singularity, and its topological charge is defined by the quantized winding angle of the vector field [1]. Vortices are widely known in hair whorls as the winding of hair strings, in fluid dynamics as the winding of velocities, in vector beams as the winding of states of polarization [2–4], and in superconductors and superfluids as the winding of order parameters [5]. Vortices are one of the most common topological excitations in nature, but they have hardly been observed other than those in the real space. Although band degeneracies, such as Dirac cones, can be viewed as momentum-space vortices in their mathematical structures, there lacks a well-defined physical observable whose winding number is an arbitrary signed integer [6].

It was recently theoretically proposed that photons in photonic crystal slabs can support vortices with a winding far-field polarization vector in momentum space [7]; multiple vortices can exist at momentum points across the first Brillouin zone (FBZ), not necessarily at the band edge [8,9]. The Bloch state at the vortex core may cease to radiate and be called a bound state in the radiation continuum [10–25]. Moreover, these momentum-space vortices could be a general phenomenon in vector fields, radiative or not. They point to a promising avenue for exploring topological properties in optics [26–31] as well as for rendering vector beams [32], but such polarization vortices have not been experimentally observed so far.

In this Letter, we experimentally demonstrate momentum-space polarization vortices in two-dimensional (2D) plasmonic crystals at visible wavelengths. The plasmonic crystals studied are flat metallic substrates coated with periodically corrugated thin dielectric layers fabricated using electron-beam lithography. The metallic substrate is a 200-nm-thick silver film evaporated on a glass substrate, and the periodic dielectric layer is a 70-nm-thick polymethyl methacrylate (PMMA) thin film (refractive index of 1.5) with a square array of cylindrical air holes (periodicity, 400 nm; hole diameter, 290 nm). Atomic force microscope images are shown in Supplemental Material [33]. The metallic film is thick enough to avoid transmission. Because of the periodicity of the PMMA array, the surface plasmon polaritons (SPPs) show well-defined band structures, and modes above the air light cone can couple into the free space and radiate [34]. Note that there is no guided mode in the wavelength region of interest. If the PMMA film is thick enough, guided modes will show a

redshift in frequency and intersect with SPP modes, forming complex band structures of hybrid SPPs.

In Fig. 1(a), we plotted the band structure of the sample, calculated using the finite-difference-time-domain method. Vortices of the far-field polarization vectors robustly exist on each dispersion band, of which the topological charges are defined by the winding angle of the vectors divided by 2π. Here, the polarization vector is the major radiation electric-field component projected onto the lattice plane. For those vortices at all high-symmetry points in the FBZ, we provide a general way to determine the possible charges, regardless of the core degeneracy level, using mirror eigenvalues on the mirror-invariant momentum lines. The C_{4v} lattice has three mirror-invariant lines of Γ-M-X-Γ in the FBZ, on which the mirror eigenvalues are ± 1. This means the corresponding far-field polarization vector is either parallel or perpendicular to those momentum lines. We denote these two cases as even (+) and odd (−) representations. By exhausting all possible combinations of representations on the high-symmetry lines surrounding each high-symmetry point, it is straightforward to see that all possible topological charges at Γ and M points are $4n \pm 1$. Here n is a signed integer. Similarly, the X point has C_{2v} symmetry, and its possible charges are $2n \pm 1$ or $2n$, detailed in Supplemental Material [33]. These are consistent with the previous conclusion [7]. Since one cannot distinguish the electric-field direction with its opposite due to the time-harmonic oscillations, we represent the polarization vector fields using line segments without arrows, which still allows us to precisely exhibit the vortices. We emphasize that our discussion works for both nondegenerate and degenerate states, since the representation at the vortex core is not needed for determining its charge. When the vortex core is a nondegenerate state, its polarization singularity corresponds to a nonradiative bound state in the radiation continuum (dark state). When the vortex core is a degenerate state, it can be either radiative (bright state) or nonradiative. In the degenerate and radiative case, the polarization is also ill defined at the singularity. It consists of a linear combination of all polarizations and can take any polarization in the far field.

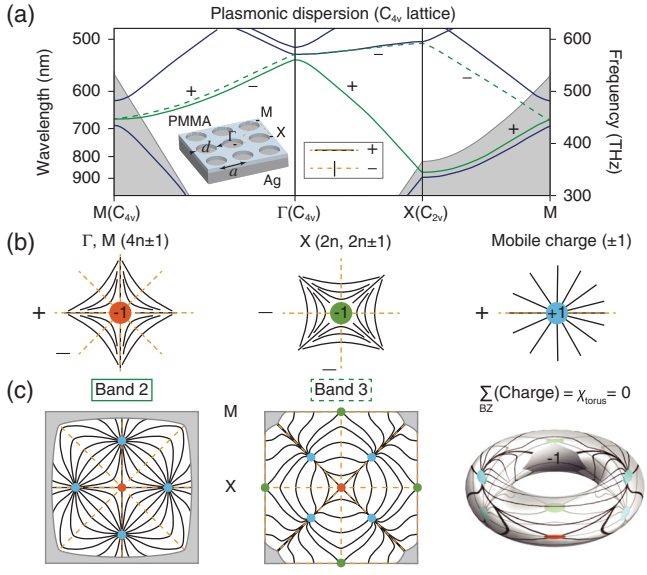

FIG. 1. (a) Simulated band structure of a plasmonic crystal with square lattice. Inset: Schematic view of the structure. The mirror eigenvalues (± 1) of modes are labeled on the high-symmetry lines. (b) Illustration of lowest-order polarization vortices at high-symmetry momentum points. The $\pm$ signs, the mirror eigenvalues along the surrounding high-symmetry lines; colored circles, the vortex cores and their charges. (c) Polarization vectors (represented by streamlines) plotted on the whole FBZ. The right panel shows the polarization streamlines on the 2D FBZ torus of band 3.

Take bands 2 and 3, for example, whose dispersion curves are plotted in Fig. 1(a) as solid and dashed green lines, respectively. Their mirror eigenvalues [see Fig. 1(a)] on Γ-M-X-Γ can be easily obtained by computing the near-field Bloch wave functions at three points—one point on each of the three mirror-invariant momentum lines (see Supplemental Material [33]). For these two bands, the possible charges at Γ and M points are $4n - 1$, and those at the X point are $2n \pm 1$. Note that bands 2 and 3 are nondegenerate on the three momentum segments excluding the end points (Γ, M, and X), so their mirror eigenvalues are constants on each momentum segment.

The sum of all vortex charges on a 2D dispersion band is zero, equaling to the Euler characteristic (χ) of the 2D FBZ torus. If the charge sum at high-symmetry points Γ, M, and X is nonzero, there must be mobile vortices inside the FBZ to neutralize the total charge. When the system parameter is continuously tuned, the mobile vortices could potentially combine at the high-symmetry points and change their n values. We computed and plotted the polarization vector fields in the whole FBZ for both bands 2 and 3 in Fig. 1(c) to illustrate our arguments. The shaded gray area indicates nonradiative states. The charges within the gray area on band 2 can be inferred to be -3 in total, and the charge at the M point on band 3 can be inferred to be -1. For the following experiments, we focus on the lowest radiative dispersion—band 2.

To experimentally characterize the band dispersions and the vortices on them, homemade polarization-resolved momentum-space imaging spectroscopy based on Fourier analysis [35] was used, as illustrated in Fig. 2(a). The working principle is the fact that the information carried by the back focal plane of an objective lens corresponds to the momentum-space (Fourier-space) information of the radiation field from the sample. There are two modes of operation. In the first mode, by positioning an imaging spectrometer, whose entrance is conjugate to the back focal plane, we map out the momentum space one line at a time within the whole visible spectrum; rotating the sample in

plane relative to the entrance slit of the imaging spectrometer yields the entire FBZ. In the second mode, we select a wavelength with a bandpass filter (10 nm bandwidth) and image the isofrequency contour in the entire FBZ onto a 2D charged-coupled-device (CCD) camera in one shot; a series of filters yield a full set of isofrequency contours. More importantly, using a polarizer, we can determine the far-field states of polarization for every momentum state. Therefore, we were able to obtain the dispersion, lifetime, and polarization of nearly all the radiative states in the whole FBZ experimentally (details in Supplemental Material [33]).

Figure 2(d) shows a 3D plot of the measured band structure of the square-lattice plasmonic crystal [image in Fig. 2(b)]. The plotted data are the extinction ratio (one minus reflectivity) as a function of the wavelength and wave vector, under unpolarized illumination and averaged over two orthogonal polarizer directions at the output. The band structure is defined by the peaks in the extinction spectra, resulting from the excitations of plasmon modes. Extinction here is directly related to radiation properties of those modes. The measured band structure agrees well with the calculation in Fig. 1(a). The key feature in Fig. 2(d) is that the extinction peaks disappear at certain momentum points (marked by the blue arrows). Since dispersion bands are physically continuous, the disappearance indicates that those states cannot be excited and are decoupled from the free space with a diverging radiative quality (Q) factor. Similar states were recently observed in dielectric photonic crystal slabs [15,21]. We measured the Q factors of nearly all the Bloch states above the light cone by fitting the experimental extinction spectra with the temporal coupled mode theory (see Supplemental Material [33]). Figure 2(e) shows the distribution of radiative Q factors on band 2 [blue dashed line in Fig. 2(d)], where a total of five vortices can be seen from the diverging Q. One vortex is fixed at Γ, and the other four are along the Γ-X lines.

The extinction spectra are polarization dependent, having the relation $E_{xt}^{(\hat{\alpha})} \sim |\hat{t} \cdot \vec{d}|^2$, where $\hat{t}$ is the effective polarizer transmission axis projected onto the $\hat{s} - \hat{p}$ plane and the polarization state of the resonant radiation is defined by $\vec{d} = d_s \hat{s} + d_p \hat{p}$. (See the derivation in Supplemental Material [36].) Thus, by changing the polarizer angle α and measuring polarization-dependent extinction spectra, we could determine the polarization states of SPP modes. We measured extinction spectra at three polarizer angles. As shown in Fig. 2(c), the polarizer angles were 0°, −45° and 90° relative to the direction of the entrance slit of the spectrometer. The details of the methods are shown in Supplemental Material [36]. In general, polarization states of radiation from SPP modes are elliptical. However, due to the 180° rotational symmetry C_2 of the structure, these polarization states are close to linear polarization [37]. In Fig. 2(f), we show the polarization ellipses of the far-field radiation. The green ellipses

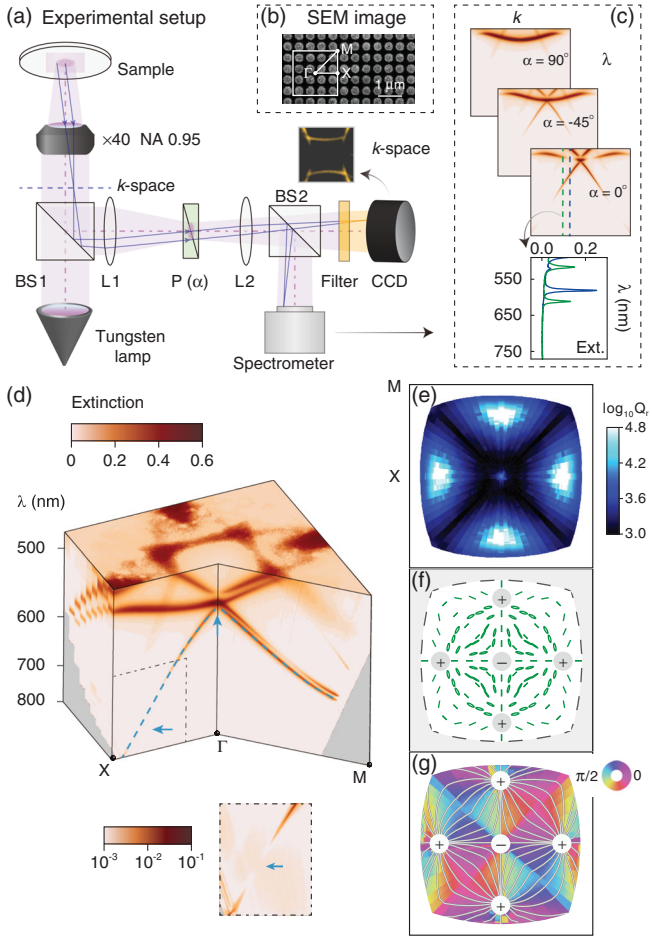

FIG. 2. (a) Schematic view of the experimental setup. BS, beam splitter; L, lens; P, polarizer. (b) SEM image of the sample. (c) Examples of polarization-dependent extinction spectra for three α. Here, the Γ-X direction of the sample is parallel to the slit of the spectrometer. (d) Measured band structure inside the FBZ. Vortices are marked with blue arrows, with a close-up on the bottom. (e) Q factors of the lowest radiative band, as highlighted by the blue dashed lines in (d). It corresponds to the green line (band 2) in Fig. 1(a). (f) Measured polarization ellipses of band 2. Vortices and their topological charges are marked with ± signs. (g) Measured angle distribution as the major axis of polarization states, represented by streamlines and colors.

and line segments above denote elliptical and linear polarizations, respectively. Figure 2(g) shows the measured polarization vector distribution as the major axis of those elliptical polarization states in the whole FBZ, plotted as streamlines on top of a pseudocolor plot. Five polarization vortices are clearly observed with one -1 vortex at Γ surrounded by four $+1$ vortices (related by the C_{4v} symmetry of the lattice). At the core of each vortex, the polarization is ill defined, indicating an absence of radiation and corresponding to the divergent Q factors in Fig. 2(e). Because of their topological nature, polarization vortices are insensitive to the variation of the structure parameters such as filling fractions and thicknesses, which we verified

experimentally in Supplemental Material [33]. The experimentally obtained topological charges are in good agreement with the theoretical prediction in Fig. 1(c).

For an even more direct visualization of the vortices in the FBZ, we use the second mode of operation and sum the isofrequency contours measured at a continuous range of wavelengths. We took a series of polarization-averaged isofrequency contours from 550 to 740 nm with a wavelength interval of 10 nm. The bandwidth of the color filters is also 10 nm, so the isofrequency contours overlap, and the whole wavelength range is covered. A few examples of the measured isofrequency contours are shown in Fig. 3(a) (the others are shown in Supplemental Material [33]). Note that only the colored contours with smaller wave vectors are from band 2, while those in light gray are from the higher bands. By summing the isofrequency contours contributed by band 2, we obtained the extinction data for the whole dispersion band and plotted it in the central figure in Fig. 3(c). Five dark regions are centered at the vortex cores with near-zero extinction in the momentum space, corresponding to the polarization vortices.

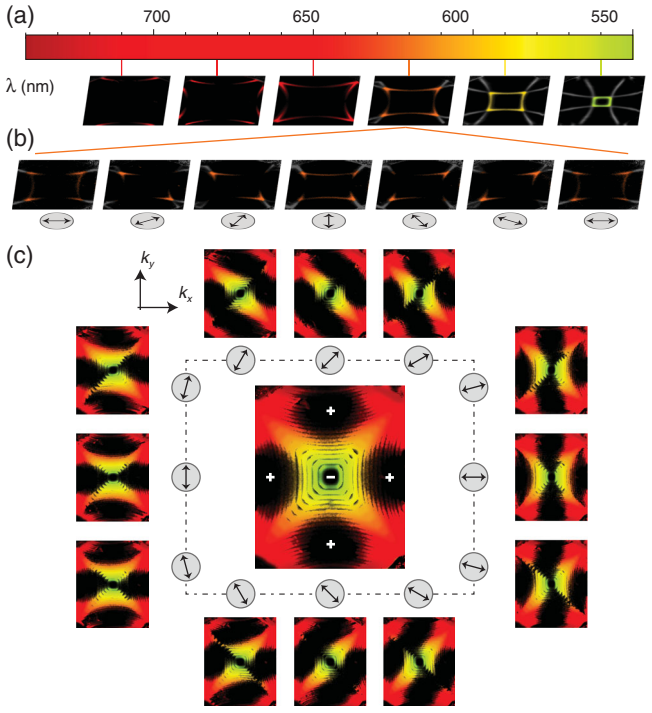

FIG. 3. (a) Examples of measured isofrequency contours under narrow-band illumination at wavelengths of 560, 590, 620, 650, 680, and 710 nm. Colored signals are from the band of interest, and light gray signals are from higher bands. (b) Examples of measured polarization-resolved isofrequency contours at 620 nm. (c) Extinction map of the band of interest in the FBZ, obtained by summing 20 isofrequency contours. Different colors correspond to different wavelengths, with the color map shown in (a). Center plot: The polarization-averaged data. Outer plots: The polarization-resolved data; the arrows aside, the direction of the polarizer.

To directly resolve the winding of polarization around the vortices, we recorded the isofrequency contours as a function of the polarizer angle, shown in Fig. 3(b). The outer plots in Fig. 3(c) show the summed isofrequency contours at different polarizer angles; the signals from states with polarization vectors perpendicular to the polarizer nearly diminish, forming a dark strip around each vortex. Those dark strips spin with the polarizer. The spinning direction and speed of them directly reveal the sign and magnitude of the topological charges. Under the counterclockwise rotation of the polarizer, the spin direction of the vortex at the Γ point is clockwise, while others spin counterclockwise. Consequently, they have opposite signs of charges. Since all five vortices rotate at the same speed as that of the polarizer, they have the same magnitude of charges of 1. This direct observation of topological charges is consistent with the numerical results in Fig. 1(c) as well as the measured polarization distribution in Fig. 2(g). Among the key experimental results of this work, an animation showing these dark strips spinning with the polarizer is presented in Supplemental Material [33].

The topological charge of a vortex can be an arbitrary signed integer. So far, we have observed ± 1 charges in the square lattice plasmonic crystal with C_{4v} point group symmetry. Higher-order charges can be realized in two ways: lattices with a higher symmetry group [7] or higher bands with a larger value of n. Here, we demonstrate both approaches.

To demonstrate the first approach, we fabricated a hexagonal lattice with C_{6v} symmetry and measured polarization-dependent isofrequency contours. As shown in the SEM image in Fig. 4(a), the structure is a 70-nm PMMA layer patterned with a hexagonal lattice on a flat silver substrate (periodicity, 600 nm; hole diameter, 330 nm). The measured band structure is shown in Fig. 4(a), while the calculation is shown in Supplemental Material [33]. Here, we picked the second band [shown as a blue dashed line in Fig. 4(a)] to observe vortices with high-order charges. The polarization distribution around the Γ point measured are shown in the central right panel in Fig. 4(b). The topological charge of this central vortex is -2. Away from Γ, there are six polarization vortices in the Γ-K directions. In the polarization-resolved isofrequency contours [outer plots in Fig. 4(b)], the dark strips of these six outside vortices rotate counterclockwise with the same angular speed as that of the polarizer, corresponding to $+1$ charges. Meanwhile, the one at the Γ point rotates clockwise with half the speed as that of the polarizer, corresponding to a vortex with -2 charge. The corresponding animation of these spinning patterns is shown in Supplemental Material [33]. Also, we fabricated a C_{4v} sample with a larger period to demonstrate the second approach. We found polarization vortices with a topological charge of -3 with $n = -1$ at the M point of band 5. Details are shown in Supplemental Material [33].

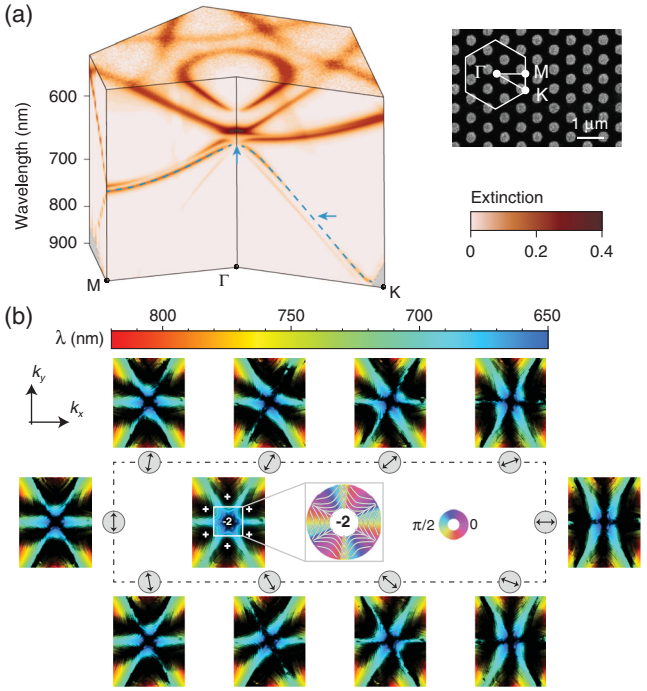

FIG. 4. (a) SEM image of the structure (right) and measured band structures using unpolarized illumination (left). Vortices are marked with blue arrows. (b) Extinction map of the band of interest [blue dashed line in (a)], obtained by summing 18 isofrequency contours. The colors correspond to different wavelengths, with the color map shown at the top. Central plots: Polarization-averaged data and measured distribution of polarization vectors near the Γ point; outer plots: polarization-resolved data; arrows aside, direction of the polarizer.

In conclusion, we have experimentally observed the momentum-space polarization vortices in the entire FBZ of plasmonic crystals. Vortices with topological charges of ± 1 and -3 were observed in a square lattice, and topological charges of -2 and $+1$ were observed in a hexagonal lattice. High-order vector beams could be generated at vortex cores of high-order momentum-space vortices, giving a promising way for on-chip applications on information encoding and optical tweezing. Such a phenomenon is generic for vector fields [45] and is an additional topological feature in band structures [26]. Transverse wave systems exhibiting polarization shall display this feature. Novel light-matter interactions could be studied by applying momentum-space polarization vortices.

We thank Chen Fang, Zhong Wang, Haiwei Yin, Shaoyu Yin, and Bo Zhen for helpful discussions. The work was supported by 973 and China National Key Basic Research Program (2015CB659400, 2016YFA0301100, 2016YFA0302000, 2017YFA0303800, and 2016YFA0302400) and National Science Foundation of China (11774063, 11727811, 11721404). The research of L. S. was further supported by Science and Technology Commission of Shanghai Municipality (17ZR1442300, 17142200100), State key laboratory of surface physics (ZA2014-01), Professor of Special Appointment (Eastern Scholar) at Shanghai Institutions of Higher Learning. L. S. and L. L. was also supported by the Recruitment Program of Global Youth Experts (1000 plans).

Y. Z., A. C., and W. L. contributed equally to this work.

*lshi@fudan.edu.cn
†linglu@iphy.ac.cn
‡jzi@fudan.edu.cn

[1] N. D. Mermin, Rev. Mod. Phys. **51**, 591 (1979).
[2] J. Nye and J. Hajnal, Proc. R. Soc. A **409**, 21 (1987).
[3] R. W. Schoonover and T. D. Visser, Opt. Express **14**, 5733 (2006).
[4] M. R. Dennis, K. O'Holleran, and M. J. Padgett, Prog. Opt. **53**, 293 (2009).
[5] J. Kosterlitz and D. Thouless, J. Phys. C **5**, L124 (1972).
[6] D. Hsieh *et al.*, Science **323**, 919 (2009).
[7] B. Zhen, C. W. Hsu, L. Lu, A. D. Stone, and M. Soljačić, Phys. Rev. Lett. **113**, 257401 (2014).
[8] E. Miyai, K. Sakai, T. Okano, W. Kunishi, D. Ohnishi, and S. Noda, Nature (London) **441**, 946 (2006).
[9] S. Iwahashi, Y. Kurosaka, K. Sakai, K. Kitamura, N. Takayama, and S. Noda, Opt. Express **19**, 11963 (2011).
[10] C. W. Hsu, B. Zhen, A. D. Stone, J. D. Joannopoulos, and M. Soljačić, Nat. Rev. Mater. **1**, 16048 (2016).
[11] D. C. Marinica, A. G. Borisov, and S. V. Shabanov, Phys. Rev. Lett. **100**, 183902 (2008).
[12] E. N. Bulgakov and A. F. Sadreev, Phys. Rev. B **78**, 075105 (2008).
[13] V. Liu, M. Povinelli, and S. Fan, Opt. Express **17**, 21897 (2009).
[14] Y. Plotnik, O. Peleg, F. Dreisow, M. Heinrich, S. Nolte, A. Szameit, and M. Segev, Phys. Rev. Lett. **107**, 183901 (2011).
[15] C. W. Hsu, B. Zhen, J. Lee, S.-L. Chua, S. G. Johnson, J. D. Joannopoulos, and M. Soljacic, Nature (London) **499**, 188 (2013).
[16] G. Corrielli, G. Della Valle, A. Crespi, R. Osellame, and S. Longhi, Phys. Rev. Lett. **111**, 220403 (2013).
[17] S. Weimann, Y. Xu, R. Keil, A. E. Miroshnichenko, A. Tünnermann, S. Nolte, A. A. Sukhorukov, A. Szameit, and Y. S. Kivshar, Phys. Rev. Lett. **111**, 240403 (2013).
[18] Y. Yang, C. Peng, Y. Liang, Z. Li, and S. Noda, Phys. Rev. Lett. **113**, 037401 (2014).
[19] M. G. Silveirinha, Phys. Rev. A **89**, 023813 (2014).
[20] F. Monticone and A. Alu, Phys. Rev. Lett. **112**, 213903 (2014).
[21] R. Gansch, S. Kalchmair, P. Genevet, T. Zederbauer, H. Detz, A. M. Andrews, W. Schrenk, F. Capasso, M. Lončar, and G. Strasser, Light Sci. Appl. **5**, e16147 (2016).
[22] A. Kodigala, T. Lepetit, Q. Gu, B. Bahari, Y. Fainman, and B. Kanté, Nature (London) **541**, 196 (2017).
[23] J. Gomis-Bresco, D. Artigas, and L. Torner, Nat. Photonics **11**, 232 (2017).
[24] Y.-X. Xiao, G. Ma, Z.-Q. Zhang, and C. T. Chan, Phys. Rev. Lett. **118**, 166803 (2017).

[25] E. N. Bulgakov and D. N. Maksimov, Phys. Rev. Lett. **118**, 267401 (2017).
[26] L. Lu, J. D. Joannopoulos, and M. Soljačić, Nat. Photonics **8**, 821 (2014).
[27] D. Leykam, M. C. Rechtsman, and Y. D. Chong, Phys. Rev. Lett. **117**, 013902 (2016).
[28] C. He, X. Sun, X. Liu, M. Lu, Y. Chen, L. Feng, and Y. Chen, Proc. Natl. Acad. Sci. U.S.A. **113**, 4924 (2016).
[29] B. Yang, Q. Guo, B. Tremain, L. E. Barr, W. Gao, H. Liu, B. Béri, Y. Xiang, D. Fan, A. P. Hibbins, and S. Zhang, Nat. Commun. **8**, 97 (2017).
[30] Y. Guo, M. Xiao, and S. Fan, Phys. Rev. Lett. **119**, 167401 (2017).
[31] Q. Wang, M. Xiao, H. Liu, S. Zhu, and C. T. Chan, Phys. Rev. X **7**, 031032 (2017).
[32] A. M. Yao and M. J. Padgett, Adv. Opt. Photonics **3**, 161 (2011).
[33] See Supplemental Material at http://link.aps.org/supplemental/10.1103/PhysRevLett.120.186103 for experimental methods, notes of temporal coupled-mode theory and supplemental figures.
[34] D. Han, F. Wu, X. Li, C. Xu, X. Liu, and J. Zi, Appl. Phys. Lett. **89**, 091104 (2006).
[35] I. De Leon and F. S. Roux, Phys. Rev. B **71**, 235105 (2005).
[36] See Supplemental Material at http://link.aps.org/supplemental/10.1103/PhysRevLett.120.186103 for the derivation on the link between polarization states and polarization-dependent extinction spectra, which includes Refs. [7,37–44].
[37] C. W. Hsu, B. Zhen, M. Soljačić, and A. D. Stone, arXiv:1708.02197.
[38] J. Korger, T. Kolb, P. Banzer, A. Aiello, C. Wittmann, C. Marquardt, and G. Leuchs, Opt. Express **21**, 27032 (2013).
[39] W. Suh, Z. Wang, and S. Fan, IEEE J. Quantum Electron. **40**, 1511 (2004).
[40] S. Fan and J. D. Joannopoulos, Phys. Rev. B **65**, 235112 (2002).
[41] S. Fan, W. Suh, and J. D. Joannopoulos, J. Opt. Soc. Am. A **20**, 569 (2003).
[42] B. Zhen, C. Hsu, Y. Igarashi, L. Lu, I. Kaminer, A. Pick, S. Chua, J. Joannopoulos, and M. Soljačić, Nature (London) **525**, 354 (2015).
[43] H. Zhou, B. Zhen, C. W. Hsu, O. D. Miller, S. G. Johnson, J. D. Joannopoulos, and M. Soljačić, Optica **3**, 1079 (2016).
[44] L. Verslegers, Z. Yu, Z. Ruan, P. B. Catrysse, and S. Fan, Phys. Rev. Lett. **108**, 083902 (2012).
[45] B.-J. Yang, M. S. Bahramy, and N. Nagaosa, Nat. Commun. **4**, 1524 (2013).

Supplemental Material

Supporting animations

Animation S1: Direct experimentally observations of polarization vortices with higher-order topological charge 3 (the value n = 1) at M point. These animations combine the individual polarization-resolved extinction maps in Fig. 3C and Fig. 4B of the main text, respectively. (One should use Acrobat Reader to view these animations.)

Materials and methods

1. Fabrications of two-dimensional (2D) plasmonic crystals

The 2D plasmonic crystal studied here is a flat silver film coated with a periodic corrugated thin polymethylmethacrylate (PMMA) layer fabricated using electron-beam lithography. The silver film was coated on a glass substrate using a thermal evaporator (Kurt J. Lesker NANO 36). The thickness of the silver film is 200 nm. A thin 70-nm PMMA layer was then spin-coated on the silver film. Desired periodic structures are written on the PMMA layer using electron-beam lithography (Zeiss Sigma 300 scanning electron microscopy plus Raith Elphy Plus).

2. Polarization-resolved momentum-space imaging spectroscopy

A home-made polarization-resolved momentum-space imaging spectroscopy was built based on an Olympus microscope (IX73). The incident light is irradiated from a tungsten lamp, focused by an objective (40× magnitude, NA 0.95) on to a sample. The back focal plane of the same objective was imaged onto the entrance slit of an imaging spectrometer using a series of convex lens. A schematic view of the setup is shown in Fig. 2A. Thus the reflected light from the sample into a given angle corresponds to a single position on the entrance slit. After the spectrometer (Princeton Instruments IsoPlane-320), the angle-resolved information, in other words the information in momentum space, is imaged with a CCD (PIXIS 400). A polarizer is placed on the focal plane of lens 1 to select a certain polarization. Normalizing the reflected light from the sample (I_s) by that from a silver mirror (I_m), we obtain the angle-resolved and polarization-resolved reflection ($R = I_s/I_m$) and extinction ($\mathrm{E_{xt}} = 1 - R$) spectra of the sample. Averaging over two orthogonal polarizer orientations yields unpolarized extinction. High extinctions arise from the excitations of the resonant modes of the structure. In the band structure measurement, one axis of the 2D CCD is used to resolve the angle of the reflected light, while the other axis is used to resolve the wavelength. The band structure $E(k)$ was subsequently calculated from the angle and wavelength resolved spectra as $E = \frac{1240}{\lambda\ (\mathrm{nm})}$ eV and $k = k_0 \sin\theta$, where $k_0 = 2\pi/\lambda$ and θ is the angle with respect to sample normal. Each measurement yields the band structure across one line Γ–Z_i of the Brillouin zone (as shown in Fig. S6) that is parallel to the entrance slit of the spectrometer. By rotating the sample in plane relative to the entrance slit of the imaging spectrometer, we obtain the band structure inside the grey regions shown in Fig. S6. Due to lattice symmetry, this yields the band structure and polarization information inside the entire Brillouin zone.

In the iso-frequency contour measurements, a narrow band-pass filter (Delta Optical Thin Film A/S) was used. The grating of the spectrometer was working on the 0th order, and the entrance slit was fully opened. Here, both axes of the 2D CCD was used to resolve the angle dependence of the extinction. As mentioned before, there is a one-to-one correspondence between the angle θ and momentum k, thus the iso-frequency contours are obtained. As in the band structure measurements, we also obtain both polarization-resolved and polarization-averaged results. With different

pass-bass filters, we obtain a series of iso-frequency contours covering the full range of dispersion of the band of interest.

Supporting notes

1. Polarization-resolved and polarization-averaged extinctions

At each angle, our system is characterized by a two-by-two field reflection matrix

$$r = \begin{pmatrix} r_{ss} & r_{sp} \\ r_{ps} & r_{pp} \end{pmatrix} \tag{S1}$$

at frequencies with no higher-order diffraction. Here r_{ps} is the coefficient of reflection into the p polarization for incident light polarized in s, and similarly for the other three elements. The two axes of polarizations are $\hat{s} = \hat{z} \times \hat{k}/|\hat{z} \times \hat{k}|$ and $\hat{p} = \hat{s} \times \hat{k}$, with $\hat{k}$ being the propagation direction and $\hat{z}$ being the normal direction of the 2D plasmonic crystal.

A polarizer is placed on the output side, oriented facing $\hat{z}$ with its transmission axis pointing along $\hat{\alpha}$ in the $\hat{x}$–$\hat{y}$ plane. For light incident along $\hat{k}$, the polarizer projects the electric field onto an effective transmission axis $\hat{t} = \hat{k} \times (\hat{\alpha} \times \hat{z})/|\hat{k} \times (\hat{\alpha} \times \hat{z})|$ in the $\hat{s}$–$\hat{p}$ plane [1]. Since the incident light in the experiment is unpolarized, we need to average over randomly polarized incident fields. The resulting polarization-resolved extinction with an unpolarized incident source is

$$\mathrm{E}_{\mathrm{xt}}^{(\hat{\alpha})} = 1 - R(\hat{\alpha}) = 1 - \left\| (\hat{t} \cdot \hat{s}, \hat{t} \cdot \hat{p}) r \right\|^2, \tag{S2}$$

where $R(\hat{\alpha})$ is the reflected intensity of the plasmonic crystal normalized by that of a mirror, both measured with a polarizer pointing along $\hat{\alpha}$. This is the main quantity measured in our experiment.

For the polarization-averaged extinction, we average over the reflectivity measured at two orthogonal polarizer orientations, yielding

$$\mathrm{E}_{\mathrm{xt}}^{(\mathrm{avg})} = 1 - \frac{R(\hat{\alpha}) + R(\hat{z} \times \hat{\alpha})}{2} = 1 - \frac{\mathrm{Tr}(r^\dagger r)}{2}. \tag{S3}$$

This is the same as the extinction measured with an unpolarized incident light and without a polarizer at the output, so we also refer to it simply as the unpolarized extinction.

2. Temporal coupled-mode theory

To relate the experimentally measured extinction to the properties of the resonances, we use temporal coupled-mode theory (TCMT) [2],

$$\begin{aligned} \frac{dA}{dt} &= (-i\Omega - \Gamma - \Gamma_{\mathrm{nr}})\, A + D^{\mathrm{T}} s^+, \\ s^- &= C s^+ + D A. \end{aligned} \tag{S4}$$

Here, A is a column vector containing the amplitudes of the resonances (N of them). We choose a basis such that the Hermitian matrix Ω is diagonal and contains the resonant frequencies, $\Omega = \mathrm{diag}(\omega_1, \ldots, \omega_N)$. Matrix Γ describes radiation loss; its diagonal elements $\{\gamma_{j,\mathrm{r}}\}_{j=1}^N$ are the radiative decay rates of the resonances, and its off-diagonal elements couple the resonances via radiation. Matrix Γ_{nr} describes non-radiative decays due to absorption, and we assume it is diagonal with $\Gamma_{\mathrm{nr}} = \mathrm{diag}(\gamma_{1,\mathrm{nr}}, \ldots, \gamma_{N,\mathrm{nr}})$. The column vectors $s^+ = (s_s^+, s_p^+)^{\mathrm{T}}$ and $s^- = (s_s^-, s_p^-)^{\mathrm{T}}$ contain the amplitudes of the incident and reflected light (with T denoting matrix transpose), which are coupled to the resonances via the coupling coefficients (*i.e.*, radiation coefficients)

$$D = \begin{pmatrix} d_{s1}, & d_{s2}, & \cdots & , d_{sN} \\ d_{p1}, & d_{p2}, & \cdots & , d_{pN} \end{pmatrix}. \tag{S5}$$

Energy conservation requires that $D^\dagger D = 2\Gamma$. Finally, $C = \exp[i\, \mathrm{diag}(\theta_s^{(\mathrm{d})}, \theta_p^{(\mathrm{d})})]$ is the reflection matrix for the direct (non-resonant) response and can be modeled by that of a homogeneous dielectric slab [3, 4] on a silver substrate; C is unitary since the absorption in this case is negligible. The resulting reflection matrix at frequency ω, including both direct and resonant reflections, is [5]

$$r = \left[I - iD(\omega - H_{\mathrm{eff}})^{-1} D^\dagger \right] C = \left[I - 2W(2 + W)^{-1} \right] C, \tag{S6}$$

where $H_{\text{eff}} = \Omega - i\Gamma - i\Gamma_{\text{nr}}$ and $W \equiv iD(\omega - \Omega + i\Gamma_{\text{nr}})^{-1}D^{\dagger}$. Note that Eq. (S4) is only valid when the periodic structure has 180-degree rotational symmetry C_2, but Eq. (S6) remains valid without C_2 symmetry [6].

3. Extraction of Q factors from extinction data

To extract the quality factors of the resonances, we use the measured unpolarized extinction spectra. The detailed extinction line shape depends on the polarization states of radiation from all N resonances [7] and has more parameters than we need. Since the quality factors are not sensitive to the detailed line shape, we make an approximation that each resonance couples only to s-polarized or only to p-polarized far field. This approximation becomes exact along the high-symmetry lines Γ–M–X–Γ and is accurate whenever the resonances are sufficiently spectrally separated (for which the polarization dependence drops out after polarization averaging). Then $W = \text{diag}(2f_s, 2f_p)$ with

$$f_s \equiv \sum_{j\in s} \frac{i\gamma_{j,\text{r}}}{\omega - \omega_j + i\gamma_{j,\text{nr}}}, \quad f_p \equiv \sum_{j\in p} \frac{i\gamma_{j,\text{r}}}{\omega - \omega_j + i\gamma_{j,\text{nr}}}, \tag{S7}$$

where $\sum_{j\in s}$ denotes a summation over the resonances that couple to s polarization, and similarly for $\sum_{j\in p}$. Inserting Eqs. (S6)–(S7) into Eq. (S3) yields

$$\text{E}_{\text{xt}}^{(\text{avg})} = 1 - \frac{1}{2}\left(\left|\frac{1-f_s}{1+f_s}\right|^2 + \left|\frac{1-f_p}{1+f_p}\right|^2\right). \tag{S8}$$

By fitting the experimental extinction spectra to Eq. (S8) at each wavevector $\mathbf{k}_{\parallel}$, we extract the resonant frequency ω_j, radiative Q factor $Q_{j,\text{r}} = \omega_j/(2\gamma_{j,\text{r}})$, and non-radiative Q factor $Q_{j,\text{nr}} = \omega_j/(2\gamma_{j,\text{nr}})$. This also yields the total Q factor $Q_{j,\text{tot}} = (Q_{j,\text{r}}^{-1} + Q_{j,\text{nr}}^{-1})^{-1}$. Fig. S4 shows the extracted Q factors, as well as comparisons between the measured and the fitted extinction curves.

4. Extraction of polarization vector fields from extinction data

To extract the polarization state of the band of interest, we use the measured polarization-resolved extinction spectra. To simplify the analytic expression, we only consider the resonance of interest, with resonance frequency ω_0, radiative decay rate γ_{r}, non-radiative decay rate γ_{nr}, and coupling coefficients $D = (d_s, d_p)^{\text{T}}$. Inserting Eq. (S6) into Eq. (S2), we get

$$\text{E}_{\text{xt}}^{(\hat{\alpha})} = \frac{2\gamma_{\text{nr}}|\hat{t}\cdot\vec{d}|^2}{(\omega-\omega_0)^2 + (\gamma_{\text{r}}+\gamma_{\text{nr}})^2}, \tag{S9}$$

where $\vec{d} = d_s\hat{s} + d_p\hat{p}$. Recall that the resonant radiation into s and p polarizations are d_sA and d_pA, as seen in Eq. (S4). Therefore, from the polarization-resolved extinction measured at different polarizer orientations $\hat{\alpha}$, we can determine the polarization state of the resonant radiation as defined by $\vec{d}$.

We measure the extinction with the polarizer's in-plane transmission axis $\hat{\alpha}$ being in the $\hat{x}$–$\hat{y}$ plane at $-\alpha_{\text{slit}}$ relative to the entrance slit of the imaging spectrometer (namely, relative to $\mathbf{k}_{\parallel}$ along the Γ–Z_i direction). We define $\gamma = \arccos(\hat{k}_{\parallel}\cdot\hat{x})$ to be the angle between the Γ–Z_i and the Γ–X directions in momentum space, as shown in Fig. S5. We carry out three measurements with α_{slit} being 0°, 45°, and 90°. The schematic view of the measurement and some representative measured data are shown in Fig. S5 and Fig. S6. At these three angles, $\hat{\alpha} = \hat{k}_{\parallel}$, $(\hat{k}_{\parallel} - \hat{s})/\sqrt{2}$, $\hat{s}$, and the effective transmission axis $\hat{t}$ is $\hat{p}$, $[(\hat{k}_{\parallel} - \hat{s})\cos\theta - \hat{z}\sin\theta]/[\sqrt{1+\cos^2\theta}]$, $\hat{s}$, respectively. From Eq. (S9), we get

$$\frac{\text{E}_{\text{xt}}^{0^\circ}}{|d_p|^2} = \frac{\text{E}_{\text{xt}}^{45^\circ}}{|d_p - d_s\cos\theta|^2/(1+\cos^2\theta)} = \frac{\text{E}_{\text{xt}}^{90^\circ}}{|d_s|^2}, \tag{S10}$$

where $\theta = \arccos(\hat{k}\cdot\hat{z}) \in [0, \pi/2]$ is the reflected (or incident) angle.

We want to determine the angle ϕ_{s-p} of the polarization vector $\vec{d}$ in the $\hat{s}$–$\hat{p}$ plane, as defined by $\tan\phi_{s-p} = d_s/d_p$. When $\vec{d}$ is linearly polarized, solving Eq. (S10) yields

$$\tan\phi_{s-p} = \frac{\sqrt{\text{E}_{\text{xt}}^{90^\circ}/\text{E}_{\text{xt}}^{0^\circ}}}{\cos\theta_{sp}}, \tag{S11}$$

where

$$\cos\theta_{sp} = \frac{\Re(d_s^* d_p)}{|d_s d_p|} = \frac{\text{E}_{\text{xt}}^{0^\circ} + \text{E}_{\text{xt}}^{90^\circ}\cos^2\theta - \text{E}_{\text{xt}}^{45^\circ}(1+\cos^2\theta)}{2\cos\theta\sqrt{\text{E}_{\text{xt}}^{0^\circ}\text{E}_{\text{xt}}^{90^\circ}}}. \tag{S12}$$

It was recently pointed out that $\vec{d}$ may deviate slightly from linear polarization away from the high-symmetry lines, and that a linearly polarized vector can still be defined via $d'_s = d_s$ and $d'_p = d_p[r_s^{(\mathrm{d})}/r_p^{(\mathrm{d})}]^{1/2}$, $d'_p = d_p \exp[i(\theta_s^{(\mathrm{d})} - \theta_p^{(\mathrm{d})})/2]$ (Ref. [8]). Here $\theta_s^{(\mathrm{d})}$ and $\theta_p^{(\mathrm{d})}$ are the reflection phase shifts of the direct (non-resonant) response as mentioned in the definition of matrix C above; they are modeled as that of a dielectric film on silver substrate. To account for this deviation, we use the angle ϕ'_{s-p} given by

$$\tan \phi'_{s-p} \equiv \frac{d'_s}{d'_p} = \frac{\sqrt{\mathrm{E}_{\mathrm{xt}}^{90^\circ}/\mathrm{E}_{\mathrm{xt}}^{0^\circ}}}{\cos(\theta_{sp} + \delta\theta_{sp})}, \tag{S13}$$

where $\delta\theta_{sp} = (\theta_s^{(\mathrm{d})} - \theta_p^{(\mathrm{d})})/2$ is from the reflection phase shifts of a dielectric film on silver substrate. These equations are for the general case when neither $\mathrm{E}_{\mathrm{xt}}^{0^\circ}$ nor $\mathrm{E}_{\mathrm{xt}}^{90^\circ}$ is zero; when one of them is zero (*e.g.*, on high-symmetry lines), ϕ'_{s-p} is simply $\pi/2$ or 0. Note that the angle ϕ'_{s-p} is only determined up to modulo π since physically one cannot distinguish between a polarization state of $\vec{d}$ versus $-\vec{d}$.

Since the $\hat{s}$–$\hat{p}$ plane rotates with $\mathbf{k}_\parallel$, we project the polarization vector onto the $\hat{x}$–$\hat{y}$ plane [9]. We determine the projected angle with the geometric relation

$$\phi = \gamma + \phi_{\mathrm{slit}} = \gamma + \arctan\left(\frac{\tan \phi'_{s-p}}{\cos\theta}\right), \tag{S14}$$

where ϕ_{slit} is the angle between the projected polarization vector and the entrance slit direction, as shown in Fig. S5.

[1] J. Korger, T. Kolb, P. Banzer, A. Aiello, C. Wittmann, C. Marquardt, and G. Leuchs, Opt. Express **21**, 27032 (2013).
[2] W. Suh, Z. Wang, and S. Fan, IEEE J. Quantum Electron. **40**, 1511 (2004).
[3] S. Fan and J. D. Joannopoulos, Phys. Rev. B **65**, 235112 (2002).
[4] S. Fan, W. Suh, and J. D. Joannopoulos, J. Opt. Soc. Am. A **20**, 569 (2003).
[5] B. Zhen, C. Hsu, Y. Igarashi, L. Lu, I. Kaminer, A. Pick, S. Chua, J. Joannopoulos, and M. Soljačić, Nature **525**, 354 (2015).
[6] H. Zhou, B. Zhen, C. W. Hsu, O. D. Miller, S. G. Johnson, J. D. Joannopoulos, and M. Soljačić, Optica **3**, 1079 (2016).
[7] L. Verslegers, Z. Yu, Z. Ruan, P. B. Catrysse, and S. Fan, Phys. Rev. Lett. **108**, 083902 (2012).
[8] C. W. Hsu, B. Zhen, M. Soljačić, and A. D. Stone (2017), arXiv: 1708.02197.
[9] B. Zhen, C. W. Hsu, L. Lu, A. D. Stone, and M. Soljačić, Physical Review Letters **113**, 257401 (2014).

Supporting figures

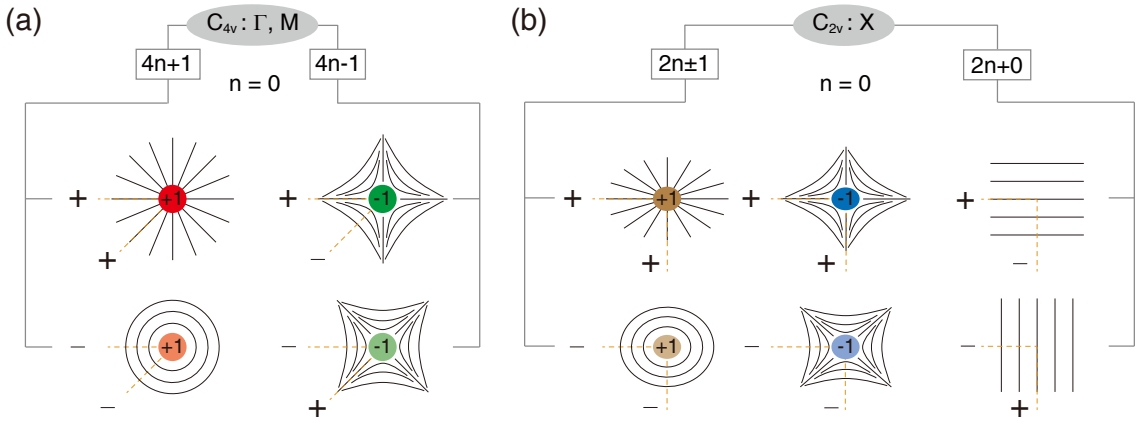

FIG. S1: **All possible topological charges of the polarization vortices located at high-symmetry points.** The possible topological charges at high-symmetry points can be determined only by the directions of those polarization vectors on the high-symmetry lines. Due to the fact that rotating polarization vectors by multiple times of π from one to the other high-symmetry line is allowed, an arbitrary integer n appears. (a) All possible topological charges of those polarization vortices at Γ and M points are shown, which can be $4n \pm 1$ with n an integer. The configurations of vortices around Γ and M points in the case of $n = 0$ are also shown. (b) Allowed charges at X point are $2n \pm 1$ and $2n + 0$. The configurations of vortices around X point ($n = 0$) are shown. Note that "0" charge is allowed here. What should be pointed out is that even though the sets of integers obtained from $4n \pm 1$ and $2n \pm 1$ are the same, 4 here represents the rotational symmetry of order 4 and the $+/-$ here refer to different symmetry class of topological charges so that $4n \pm 1$ and $2n \pm 1$ should be used for different symmetries. The $4n \pm 1$ sign should also be taken as the sign of n.

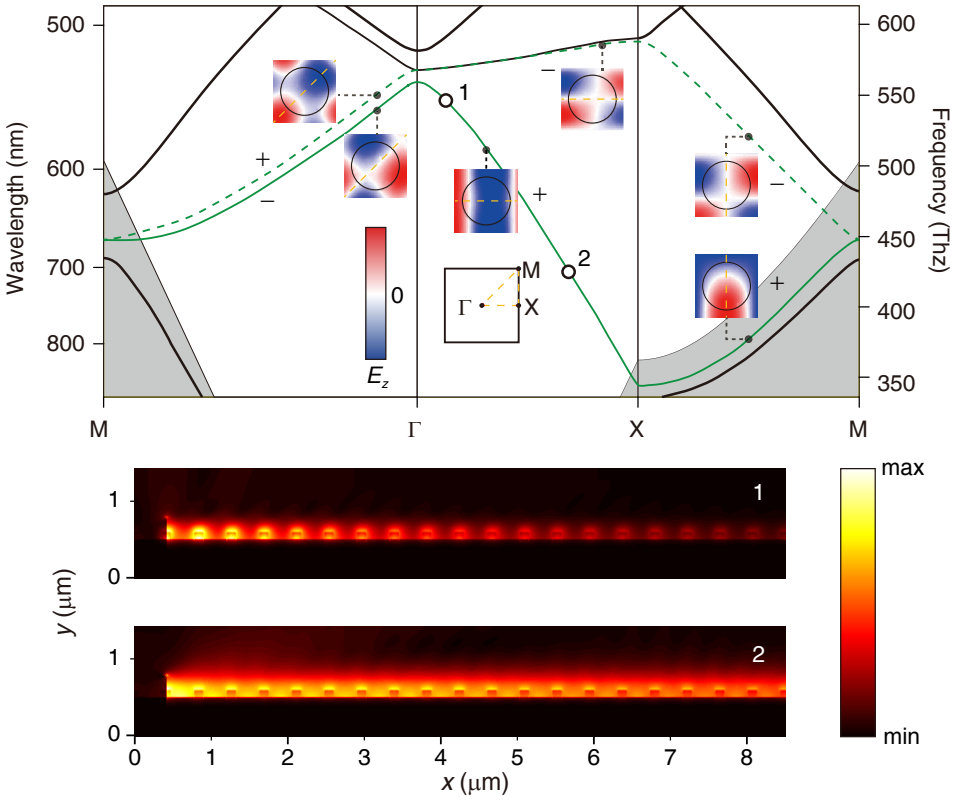

FIG. S2: Upper panel: Band structures, field distributions and mirror eigenvalues along M-Γ-X-M. Lower panel: Distributions of the magnitude of electric fields in the plane perpendicular to the silver surface along Γ-X for mode 1 (indicated in upper panel) and mode 2 (indicated in upper panel) respectively. It is clearly shown that due to the fact that mode 2 is around a bound state in the radiation continuum (a vortex core), the propagation distance is much longer than mode 1.

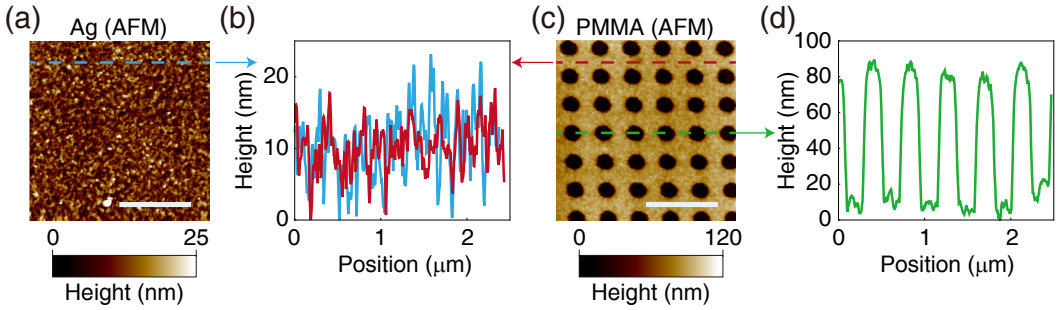

FIG. S3: **Atomic force microscope (AFM) measurement of samples used in the experiment.** The thickness of PMMA is about 70nm. The root-mean-square (rms) roughness of bare silver layer is 4.7 nm, and the rms roughness of PMMA film coated on the silver layer is 4.9 nm. The consistency of roughness suggests that the PMMA is coated on silver layer very well. (a) AFM image of bare silver layer. (b) Height profiles along blue and red dashed lines in (a) and (c), respectively. (c) AFM image of silver layer coated with periodically corrugated PMMA film. (d) Height profile along the green dashed line in (c).

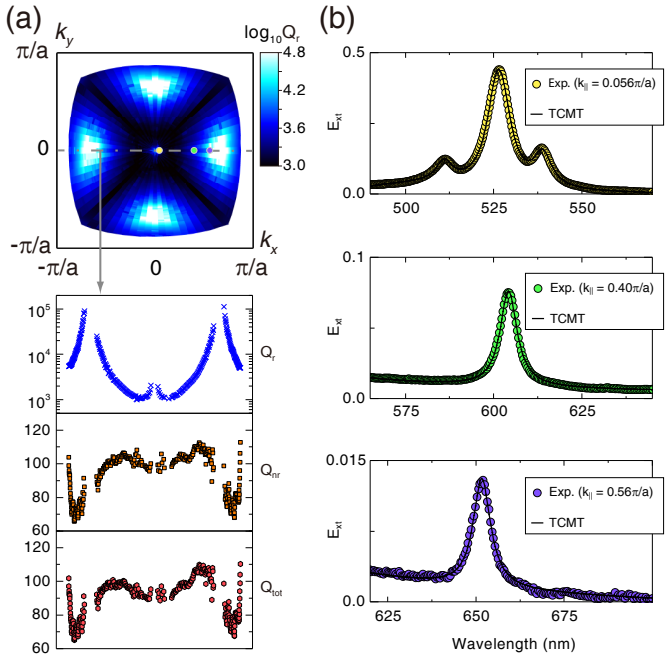

FIG. S4: **Extracted Q factors from the experimental extinction spectra.** (a) The measured momentum space distribution of radiative Q factors in whole Brillouin zone of band 2 (the upper panel). The distribution of radiative, non-radiative and total Q factors along the Γ-X direction (the grey dashed line) are shown in the lower panel. Detailed extinction spectra shown in (b) were selected at three different wavevectors along Γ-X direction marked as the yellow, green and purple dots. (b) Experimental extinction spectra at three different wavevectors alone Γ-X direction, $0.056\pi/a$ (yellow dots), $0.4\pi/a$ (green dots) and $0.56\pi/a$ (purple dots) as well as the fitting curves with TCMT (the black lines) are shown.

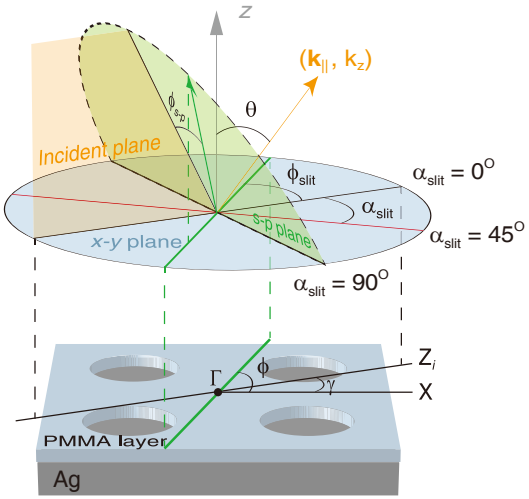

FIG. S5: Schematic illustration for the relevant angles and vectors in determining the polarization vector and its projection onto the $\hat{x}$–$\hat{y}$ plane.

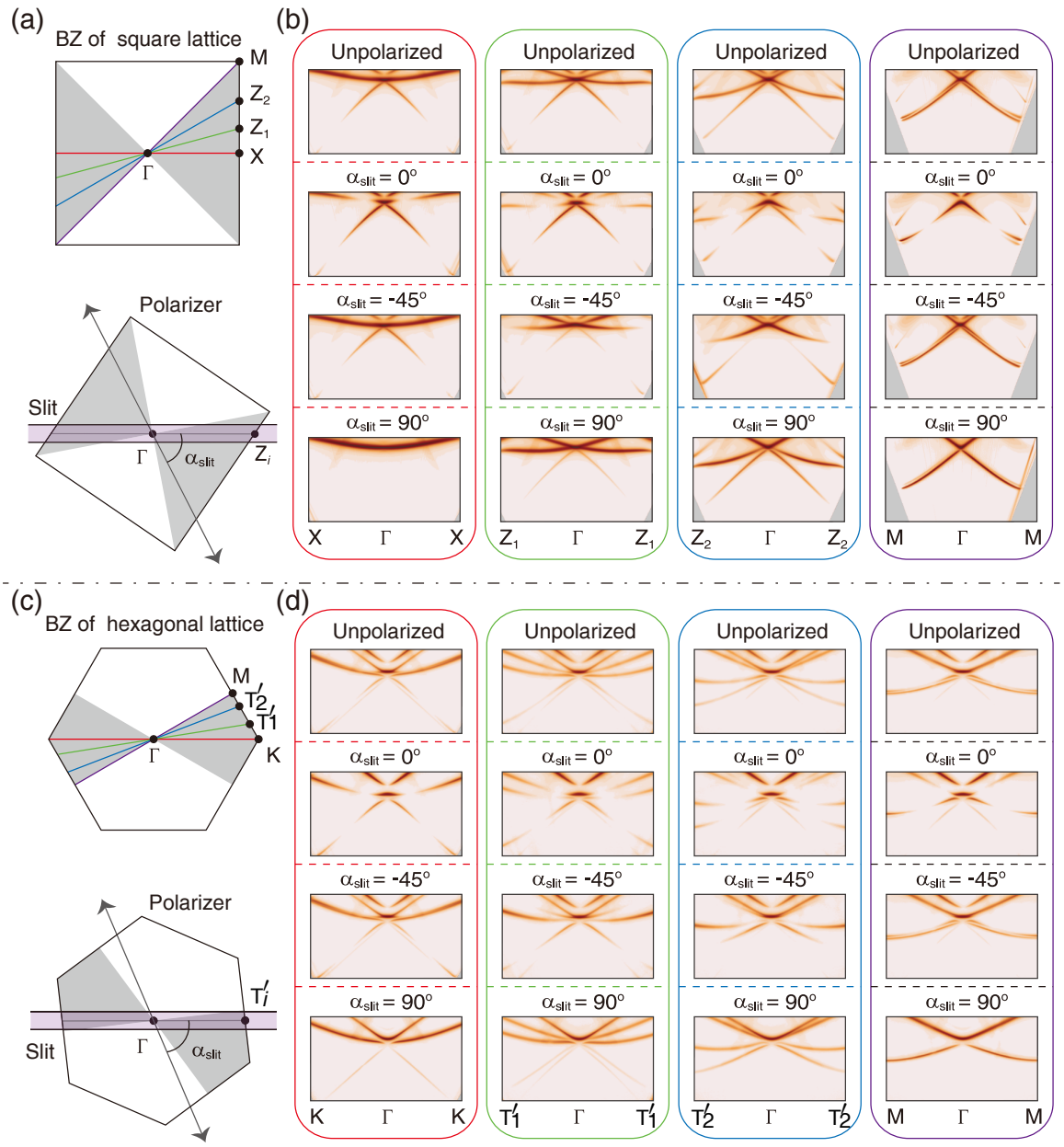

FIG. S6: **Examples of measured polarization dependent band structures along different in-plane orientations of samples.** (a) Schematic views of the Brillouin zone of square lattice and the definition of the direction of the polarizer with respect to the direction of the entrance slit of the spectrometer are shown in the upper and lower panels. (b) The measured band structures as the unpolarized (upper) and polarization-resolved (lower) extinction spectra ($\alpha_{\rm slit} = 0°, 45°, 90°$) along four in-plane orientations (marked as the red, green, blue and purple lines in (a)). (c), (d) The same as (a), (b) for the case of the hexagonal lattice.

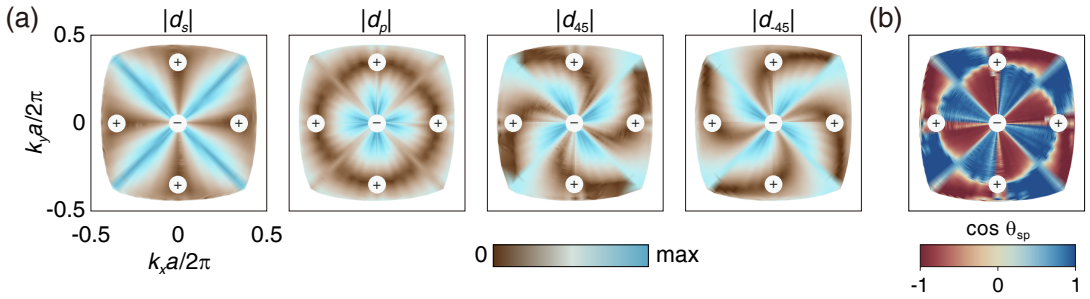

FIG. S7: (a) The measured amplitudes of coupling coefficients for s-, p- and $\pm 45°$ (another pair of mutually orthogonal) components of far-field radiation for the sample in the main text. (b) The measured data of $\cos\theta_{sp}$ representing phase difference of radiation between s polarization and p polarization.

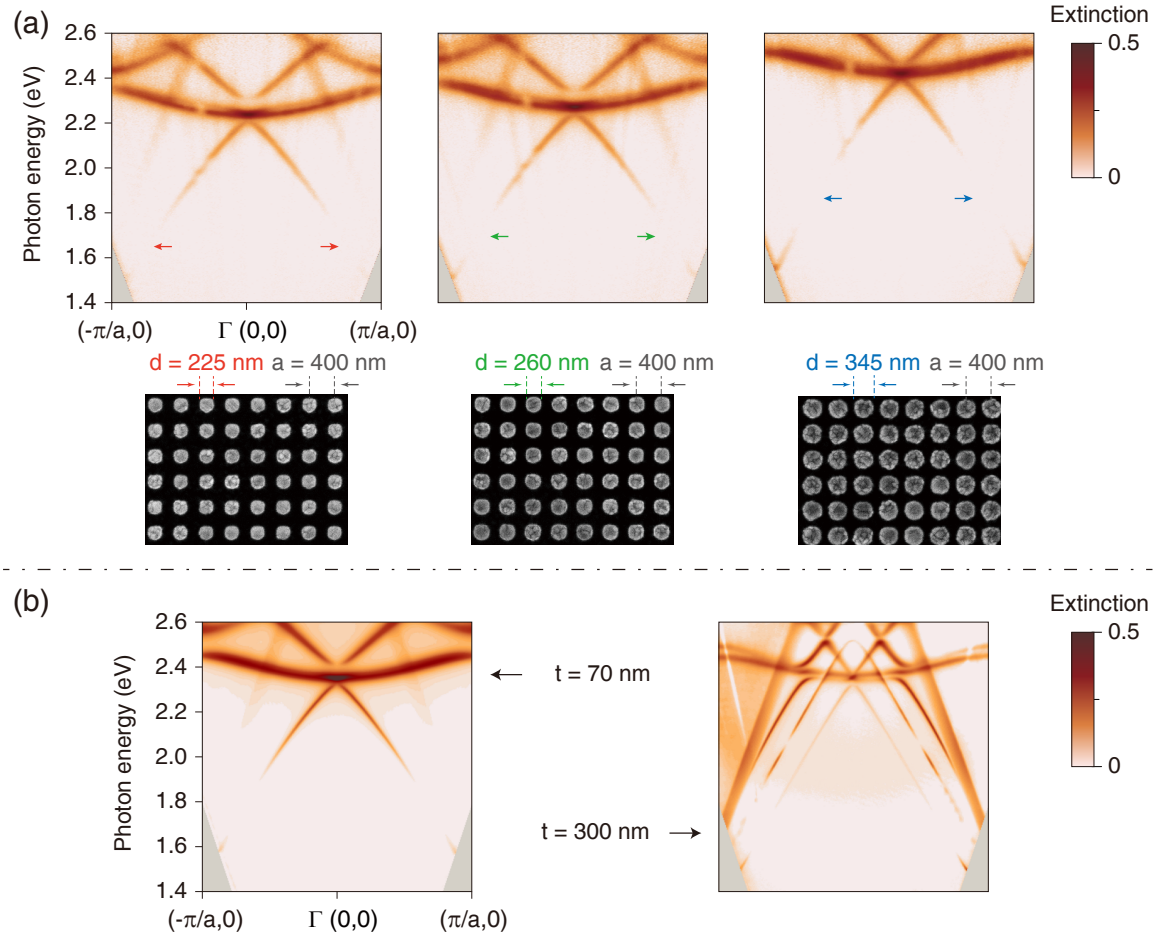

FIG. S8: (a) The robustness of optical vortices in momentum space under the variations of the filling fraction of the structures. Upper panel: the measured band structures of three samples with different filling fractions along Γ-X direction are shown. For all the three samples, the lowest bands (band 2) are disconnected, indicating the appearances of the vortices and bound states in the radiation continuum, denoted by red, green and blue arrows, respectively. Lower panel: the corresponding SEM images. All three samples have the same periodicity, a = 400 nm and the same thickness of the PMMA film, 70 nm. (b) The robustness of polarization vortices in momentum space under the variations of the thickness of the PMMA film. The measured band structures of two samples with different thicknesses of PMMA films along Γ-X direction are shown. Thicknesses of the PMMA films increase from left to right, which are 70 and 300 nm, respectively. For both samples, disconnected band structures demonstrate robust existence of polarization vortices. Increasing thickness leads to redshift in frequency of guided modes. Guided modes could couple with SPP modes, resulting in hybrid SPP modes which appear as anti-crossing of guided bands and SPP bands. To be noted that, bound states in continuum (also polarization vortices) could also appear in guided bands, similarly causing discontinuity in band structures.

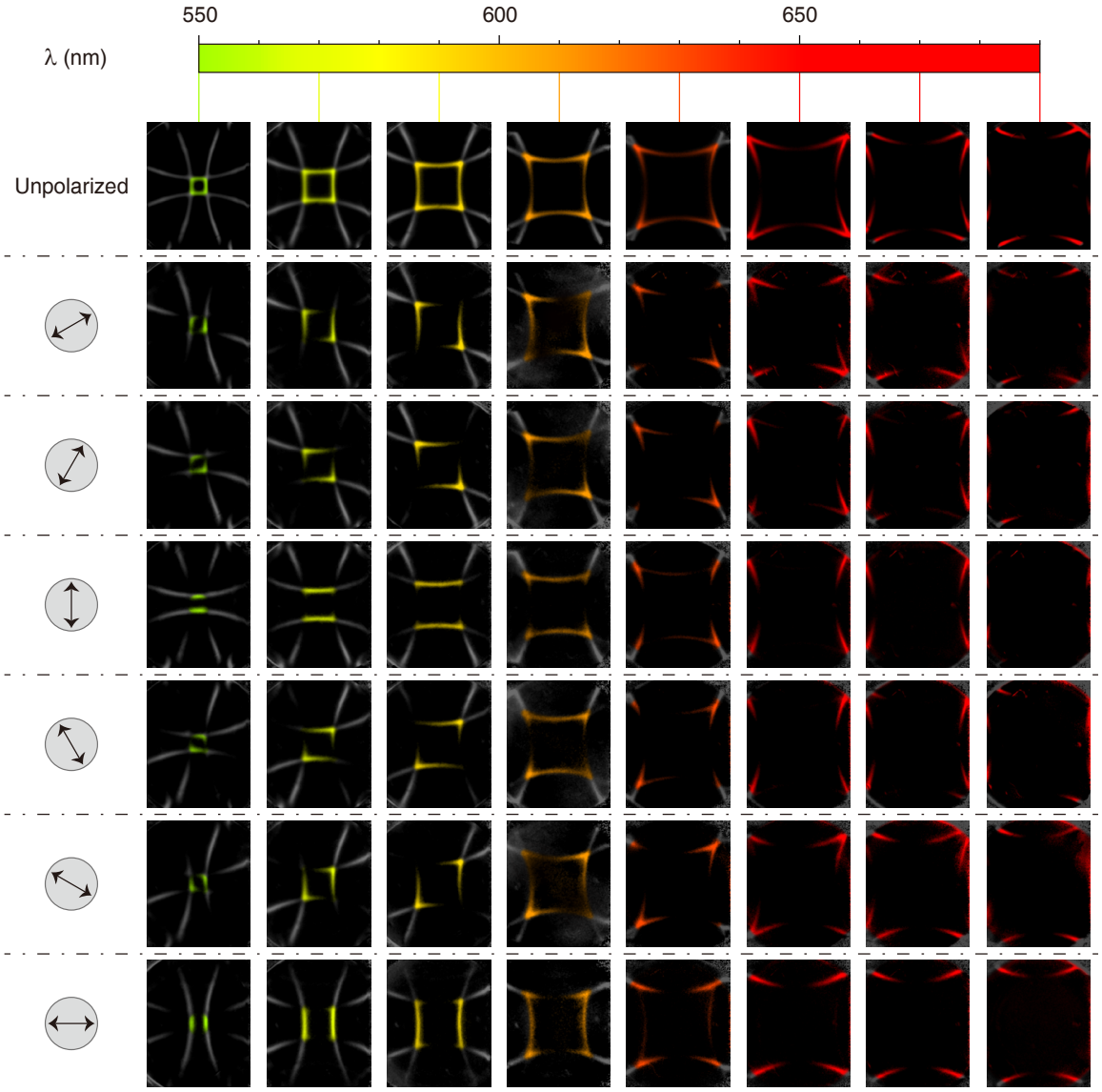

FIG. S9: Polarization-resolved iso-frequency contours of the square lattice sample. The colored parts of contours correspond to the band of interest.

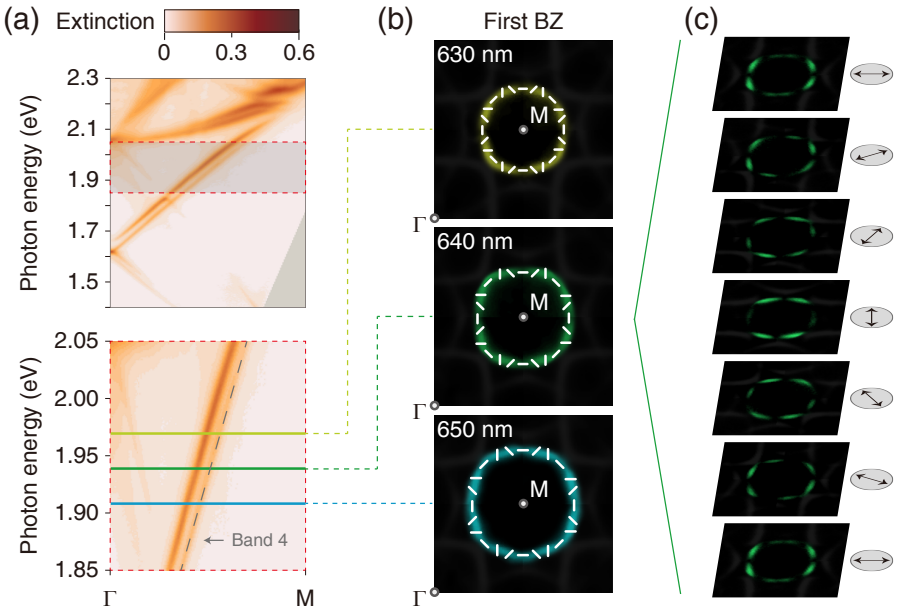

FIG. S10: **Experimental observation of polarization vortices with higher-order topological charge −3 (the value $n = -1$) at M point.** The periodicity is 650 nm; the hole diameter is 320 nm and the thicknesses of the silver film and the dielectric film ($n = 1.5$) are 200 nm and 80 nm, respectively. (a) Measured band structure along Γ-M direction. Band 4 focused on is marked with gray dashed line in the zoomed band structure on the bottom. (b) Three examples of measured polarization-averaged iso-frequency contours at wavelengths of 630, 640, 650 nm respectively, and the corresponding angle distributions as major axis of the polarization states (denoted by white line segments) are shown above. M point is positioned at the center of the first Brillouin zone in order to observe the vortex clearly. (c) Examples of measured polarization-resolved iso-frequency contours at 640 nm.

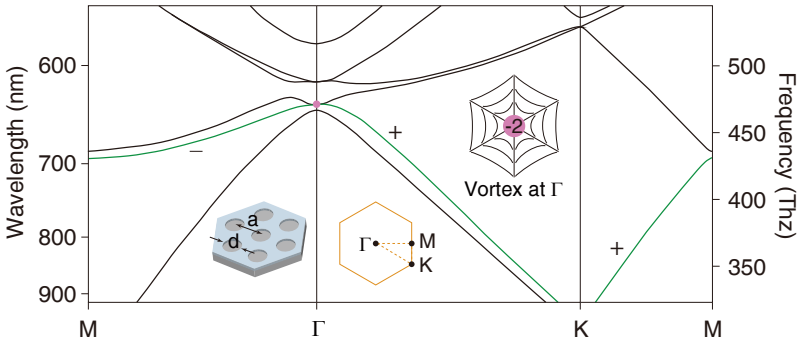

FIG. S11: Calculated band structures of a plasmonic crystal with hexagonal lattice structure by FDTD methods. The periodicity a is 600 nm; the hole diameter d is 330 nm and the thicknesses of the silver film and the dielectric film ($n = 1.5$) are 200 nm and 70 nm, respectively. The polarization directions of modes along high symmetric lines, even (+) or odd (−) are also indicated just beside the corresponding bands. The second band discussed in detail in Fig. 4 is marked as green line, and the configuration of the lowest-order vortex (marked as pink dot) located at Γ point are also shown.

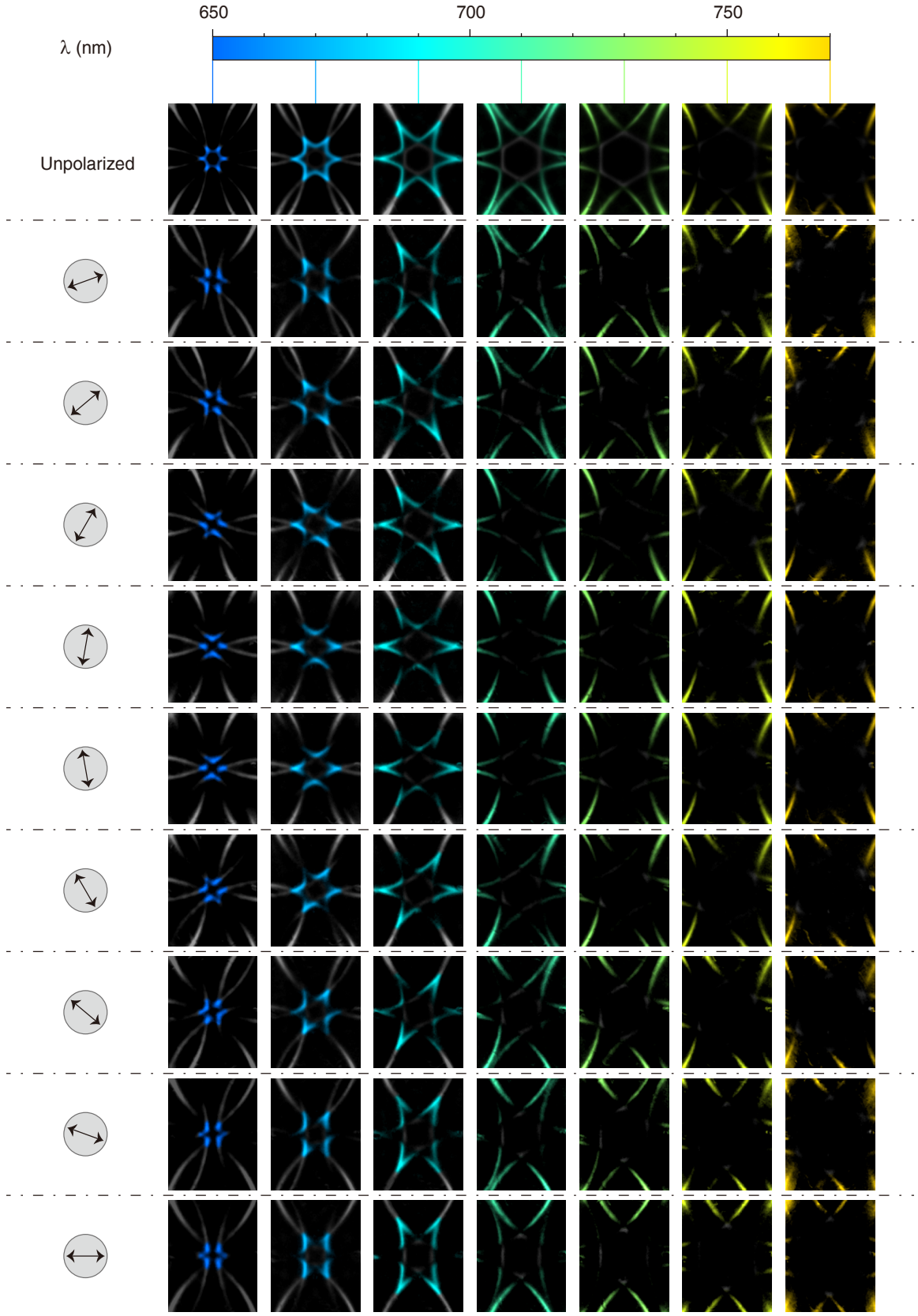

FIG. S12: The same as Fig. S10 for the hexagonal lattice sample.